A&A 582, A2 (2015)
DOI: 10.1051/0004-6361/201424724

Astronomy & Astrophysics

870 μm continuum observations of the bubble-shaped nebula Gum 31⋆

N. U. Duronea[1,2], J. Vasquez[1,2], L. Gómez[3,5], C. E. Cappa[1,2], V. Firpo[4], C. H. López-Caraballo[4], and M. Rubio[5]

[1] Instituto Argentino de Radioastronomía, CONICET, CCT-La Plata, C.C.5., 1894 Villa Elisa, Argentina
e-mail: duronea@iar.unlp.edu.ar
[2] Facultad de Ciencias Astronómicas y Geofísicas, Universidad Nacional de La Plata, Paseo del Bosque s/n, 1900 La Plata, Argentina
[3] CSIRO Astronomy and Space Science, PO Box 76, NSW 1710 Epping, Australia
[4] Departamento de Física y Astronomía, Universidad de La Serena, Av. Juan Cisternas 1200 Norte, La Serena, Chile
[5] Departamento de Astronomía, Universidad de Chile, Casilla 36, Santiago de Chile, Chile

Received 31 July 2014 / Accepted 25 June 2015

ABSTRACT

Aims. We present here a study of the cold dust in the close environs of the ring nebula Gum 31. We aim at deriving the physical properties of the molecular gas and dust associated with the nebula, and investigating its correlation with the star formation in the region, which was probably triggered by the expansion of the ionization front against its environment.
Methods. We make use of 870 μm emission data obtained with the Large APEX Bolometer Camera (LABOCA) to map the dust emission. The 870 μm emission provides an excellent probe of mass and density of dense molecular clouds. The obtained LABOCA image was compared to archival infrared, radio continuum, and optical images.
Results. The 870 μm emission follows the 8 μm *(Spitzer)*, 250 μm, and 500 μm (*Herschel*) emission distributions showing the classical morphology of a two-dimensional projection of a spherical shell. We use the 870 μm and 250 μm images to identify 60 dust clumps in the collected layers of molecular gas using the `Gaussclumps` algorithm. The clumps have effective deconvolved radii between 0.16 pc and 1.35 pc, masses between 70 $M_\odot$ and 2800 $M_\odot$, and volume densities between 1.1×10^3 cm^{-3} and $\sim 2.04 \times 10^5$ cm^{-3}. The total mass of the clumps is ∼37 600 $M_\odot$. The dust temperature of the clumps is in the range from 21 K to 32 K, while inside the HII region it reaches ∼40 K. The clump mass distribution for the sample is fitted by a power law $dN/d\log(M/M_\odot) \propto M^{-\alpha}$, with $\alpha = 0.93 \pm 0.28$. The slope differs from those obtained for the stellar IMF in the solar neighborhood, suggesting that the clumps are not direct progenitors of single stars/protostars. The mass-radius relationship for the 41 clumps detected in the 870 μm emission shows that only 37% of them lie in or above the high-mass star formation threshold. Most of this 37% have candidate YSOs projected inside their limits. A comparison of the dynamical age of the HII region with the fragmentation time, allowed us to conclude that the collect-and-collapse mechanism may be important for the star formation at the edge of Gum 31, although other processes may be acting simultaneously. The position of the identified young stellar objects in the region is also a strong indicator that the collect-and-collapse process is acting.

Key words. HII regions – ISM: bubbles – infrared: ISM

1. Introduction

There is now consensus that the formation of stars can be triggered by the action of HII regions on their parental molecular environment. Processes that sweep up and compress the gas and dust, like the collect-and-collapse mechanism (C&C; Elmegreen & Lada 1977) and the radiative driven implosion process (RDI; Lefloch & Lazareff 1994), may favor the triggering of star formation. Dense molecular condensations (or clumps) lying at the border of Galactic HII regions are therefore among the most likely sites for stellar births, and hence, where to look for early stages of star formation (e.g. Romero & Cappa 2009; Cappa et al. 2009; Vasquez et al. 2012; Deharveng et al. 2012; Duronea et al. 2014). In recent years, the triggered star formation process, especially the C&C mechanism, has been studied extensively at the edges of many bubble-shaped HII regions such as Sh2-104, RCW 79, Sh2-212, RCW 120, Sh2-217, and Sh2-90 (Deharveng et al. 2003, 2008, 2009; Zavagno et al. 2006, 2010; Brand et al. 2011; Samal et al. 2014), as well as in several surveys (e.g Thompson et al. 2012; Simpson et al. 2012)

Gum 31 is one of the many southern Galactic HII regions that appear as a ring at infrared (IR) wavelengths (see the upper panel of Fig. 3). The nebula, located at a distance of ∼2.5 kpc (Yonekura et al. 2005), is considered to be part of the giant Carina Nebula Complex (Preibisch et al. 2012), and is ionized by the stars HD 92206A, B, and C, which are members of the young stellar cluster NGC 3324 (Jeffers et al. 1963; Forte 1976; Walborn 1982; Baumgardt et al. 2000; Maíz-Apellániz et al. 2004). The simple morphology of Gum 31, along with the strong evidence of star formation in its environs (see below), make this object an excellent laboratory for the investigation of possible scenarios of triggered star formation. Cappa et al. (2008; hereafter CNAV08) analyzed the ionized, neutral, and molecular gas in the environs of Gum 31. Adopting a distance of 3 kpc, CNAV08 found an HI shell of ∼1500 $M_\odot$ around the nebula with a systemic velocity of −23 km s^{-1} expanding at ∼11 km s^{-1}. In addition, the authors found an associated molecular envelope ($\sim 1.1 \times 10^5$ $M_\odot$) at velocities between −27.2 km s^{-1}

⋆ The LABOCA map (data corresponding to Fig. 1; in FITS format) is only available at the CDS via anonymous ftp to cdsarc.u-strasbg.fr (130.79.128.5) or via http://cdsarc.u-strasbg.fr/viz-bin/qcat?J/A+A/582/A2

and −14.0 km s^{-1} that has probably been accumulated by the expansion of the ionized gas. The distribution of the molecular and ionized gas, along with the emission of the 8 μm-MSX band A, which include significant emission from polyciclic aromatic hydrocarbons (PAHs), suggests that a photodissociation region (PDR) was created at the interface between the ionization front and the molecular cloud. Using MSX, IRAS, and 2MASS photometric data, CNAV08 found a number of infrared young stellar object (YSO) candidates around the nebula which suggests that star formation is active in the high-density gas. As part of the Census of High- and Medium-mass Protostars (CHaMP) program, Barnes et al. (2011) surveyed the southern sky to detect massive molecular clumps using Mopra HCO$^+$(1−0) observations. The authors identified 19 molecular clumps in the region of Gum 31 (see Fig. 34 of that work). The systemic velocity of these clumps is in agreement with the velocity of the molecular gas reported by CNAV08. Ohlendorf et al. (2013; hereafter OPG13) used high sensitivity and spatial resolution WISE, *Herschel*, and *Spitzer* data to characterize the young stellar population surrounding the HII region. The authors estimated a total population of ∼5000 YSO candidates in the region, many of them observed in compact clusters and located at the inner edge of the bubble. They concluded that the C&C and RDI processes are probably taking place simultaneously at the border of the HII region. The authors based their conclusion on the size of Gum 31, which agrees with what is expected for a C&C scenario (Whitworth et al. 1994), and the presence of YSOs in its rims, which gives support to the C&C process, while the existence of YSOs in the head of pillars points to a RDI process. More recently, Vazzano et al. (2014) analyzed the distribution of the molecular gas and cold dust in the dense clump linked to IRAS 10361-5830, located in the southwestern edge of Gum 31. The authors found a dense molecular shell at ∼−25 km s^{-1} centered at the IRAS position, where star formation is active. They also found a number of cold dust clumps associated with the molecular shell.

Although a study of the interstellar medium (ISM) and the young stellar population around the whole Gum 31 nebula was performed by CNAV08, Barnes et al. (2011), and OPG13, a high spatial resolution analysis of the densest molecular gas adjacent to the edge of the HII region still remains to be done. Low-J transitions of ^{12}CO and ^{13}CO are commonly used to trace molecular clouds; however, they are often optically thick, thus probing only the outer layers of the cloud. Morover, optically thin transitions from C^{17}O and C^{18}O may fail to probe the inner densest molecular gas because they freeze out onto dust grains and deplete at high densities (Hernandez et al. 2011; Giannetti et al. 2014). In this context, optically thin dust continuum emission in the (sub)millimeter range is one of the most reliable tracers of the dense molecular gas from which the stars form. It provides a powerful tool for probing some basic physical properties of dense clouds (column density of molecular hydrogen, mass of the cloud, etc.) that are needed to unveil the physical conditions in regions where stars can form.

When an HII region expands, molecular gas and dust accumulates behind the ionization front, forming shells of dense molecular gas surrounding the ionized gas. With time these shells become massive (Hosokawa & Inutsuka 2006) and could contain cold dust that radiates in the (sub-)millimiter range. In the present study we analyze the distribution and physical properties of the dense gas and dust adjacent to the ionization front of Gum 31 using 870 μm continuum emission obtained with LABOCA at APEX 12m telescope. The 870 μm image is compared to IR, radio continuum, and optical archival images in order to perform a complete multiwavelength study of the dust and gas associated with the nebula and to derive their physical properties and conditions. Optically thin dust emission at 870 μm is usually dominated by the thermal emission from cold dust, which is contained in dense material (e.g. dense star-forming cores or filaments).

2. Observations and complementary data

The 870 μm continuum observations were carried out on October 2011 with the Large Apex BOlometer CAmera (LABOCA)[1]. LABOCA is a 295-pixel bolometer array developed by the Max-Planck-Institut für Radioastronomie (Siringo et al. 2007). The central frequency of the instrument is 345 GHz and the bandwidth is 60 GHz. The beam size (HPBW) at 345 GHz is 19.″2 (or 0.23 pc at 2.5 kpc). Observations were made using the on-the-fly (OTF) mode to map an inverted L-shaped region of the nebula where the 8 μm emission is more intense. During the observations the amount of precipitable water vapor (PWV) was between 0.16 mm and 0.24 mm. Absolute flux calibrations were achieved through observations of the planet Mars as primary calibrator for LABOCA, and the stars N207 11R and VY CMa as secondary calibrators. The uncertainty due to flux calibration was estimated to be ∼20%. The telescope focus and pointing were checked using the star η Carinae. Observations were smoothed down to a beam of 20.″0 to obtain a final average rms noise of 50 mJy beam^{-1}. The data were reduced using the Comprehensive Reduction Utility for SHARC-2 software package (CRUSH-2)[2] (Kovács 2008) following the standard procedure. The 870 μm emission image of the Gum 31 is shown in Fig. 1.

The 870 μm data were complemented with several archival data sets:

– Infrared images from the *Herschel*[3] Infrared GALactic (Hi-GAL) plane survey key program (Molinari et al. 2010). We used the 70 μm and 160 μm maps produced in the High-Level 2.5, and 250 μm and 500 μm maps produced in the High-Level 3 (combined maps from Parallel Mode observations done in both nominal and orthogonal scan directions) available in the Herschel Legacy as a standalone product. The Level 2.5 maps were produced with correctedmadmap in the MADMap software application (Cantalupo et al. 2010) with point source artifacts corrected. The pixel sizes of the two PACS maps are 3.″2 (for the 70 μm map) and 4.″5 (for the 160 μm map), as suggested in Traficante et al. (2011). The angular resolution for 70 μm and 160 μm bands are 10″and 13.″5, respectively. The Level 3 were produced from the Planck zero-point calibrated maps and the angular resolution for 250 μm and 500 μm maps are 18″and 36″. The *Herschel* interactive processing environment (HIPE v12[4]; Ott & Herschel Science Ground Segment Consortium 2010) was used to handle the maps.

[1] APEX is a collaboration between the Max-Planck-Institut für Radioastronomie, the European Southern Observatory, and the Onsala Space Observatory.

[2] http://www.submm.caltech.edu/~sharc/crush/index.html

[3] *Herschel* is an ESA space observatory with science instruments provided by European-led Principal Investigator consortia and with important participation from NASA http://www.cosmos.esa.int/web/herschel/science-archive

[4] HIPE is a joint development by the Herschel Science Ground Segment Consortium, consisting of ESA, the NASA Herschel Science Center, and the HIFI, PACS and SPIRE consortia members, see http://herschel.esac.esa.int/HerschelPeople.shtml

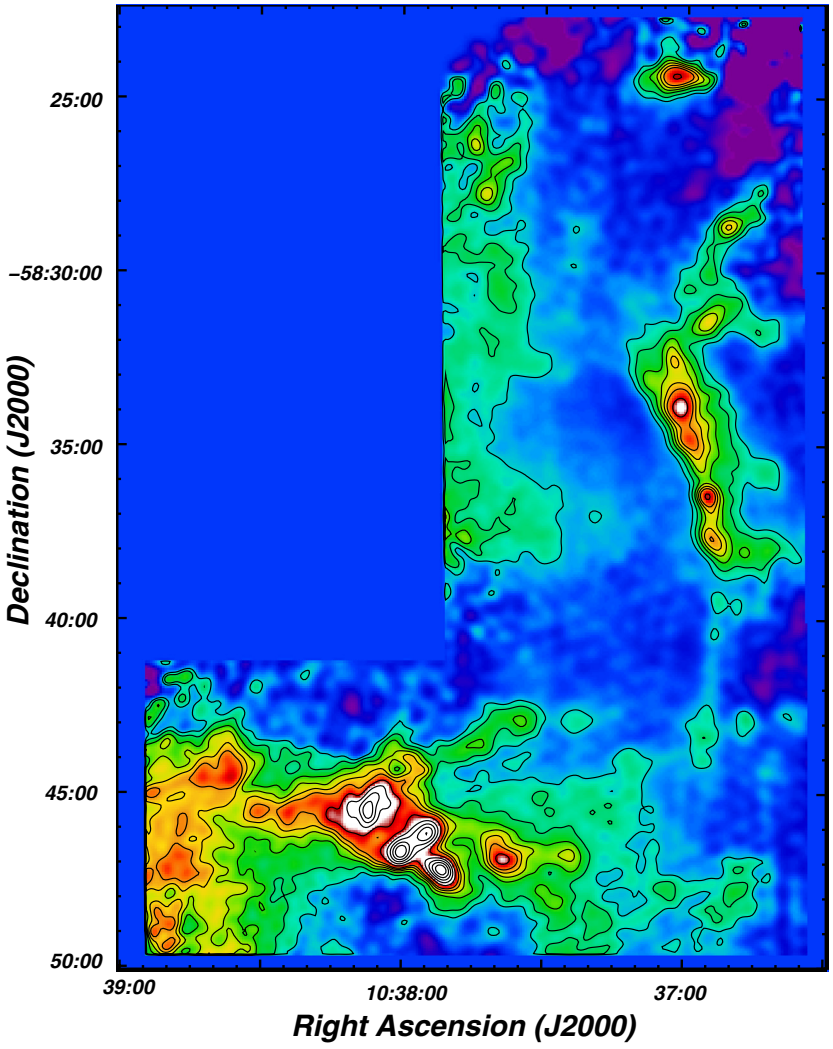

Fig. 1. 870 μm emission of Gum 31. The contours go from 150 mJy beam^{-1} ($\sim 3\sigma$) to 650 mJy beam^{-1} in steps of 100 mJy beam^{-1}, and from 650 mJy beam^{-1} in steps of 200 mJy beam^{-1}. The maximum flux density is 1860 mJy beam^{-1}.

- Infrared *Spitzer* images at 8.0 μm with a spatial resolution of $\sim 2''$, retrieved from the Galactic Legacy Infrared Mid-Plane Survey Extraordinaire (GLIMPSE)[5] (Benjamin et al. 2003).
- Radiocontinuum data from the survey of the Sydney University Molonglo Sky Survey (SUMSS)[6] (Bock et al. 1999) at 843 MHz.
- Optical data from the 2nd Digitized Sky Survey (red plate)[7] (McLean et al. 2000).

3. Observational results and discussion

3.1. 870 μm emission and comparison with other wavelengths

In Fig. 1 we show the 870 μm emission of the Gum 31 nebula. Despite the difference in spatial resolution, the 870 μm emission follows the CO(1−0) emission distribution depicted in CNAV08 (see their Fig. 5). The emission at this wavelength shows the typical IR morphology of Galactic ring nebulae (Churchwell et al. 2006, 2007; Deharveng et al. 2010) with a very intense emission towards the border of the nebula and a very faint emission towards its center. From the figure, we note that the dust emission at the border is not uniformly distributed, and several condensations can be distinguished in the whole structure. These condensations will be identified and analyzed in the next sections.

The ring morphology in the IR emission of many HII regions is a common feature in the Galaxy (e.g. Watson et al. 2008; Deharveng et al. 2009, 2010) and has originated some debate on whether these structures are flat (few parsecs) two-dimensional ring-like objects (Beaumont & Williams 2010) or three-dimensional bubbles (Deharveng et al. 2010; Anderson et al. 2012, 2015). Although it is difficult to distinguish between the two different scenarios, three observational properties suggest that the ring morphology of Gum 31 in the IR may be due to a projection effect, namely:

1) A weak structure is observed in the 870 μm emission towards the center of the nebula along RA $\approx 10^{\rm h}37^{\rm m}40^{\rm s}$ (see Fig. 1). This structure probably corresponds to IR emission of cold dust in front of the nebula, since its outer border shows an excellent spatial correlation with a region of optical absorption and 70 μm emission (see upper panel of Fig. 3). The optically absorbed region lies at RA $> 10^{\rm h}37^{\rm m}45^{\rm s}$, which leads us to conclude that there is probably more 870 μm emission, arising from the front face of the bubble in the uncovered area with LABOCA.
2) The velocity interval of the high-density molecular gas adjacent to the nebula (~ -16 km s^{-1}; Barnes et al. 2011), which

[5] http://sha.ipac.caltech.edu/applications/Spitzer/SHA
[6] http://www.astrop.physics.usyd.edu.au/cgi-bin/postage.pl
[7] http://skyview.gsfc.nasa.gov/cgi-bin/query.pl

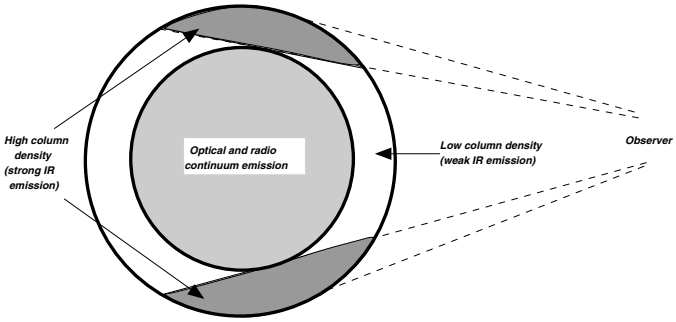

Fig. 2. Sketch of Gum 31, which could explain in a qualitative way the IR, optical, and radio continuum emission distribution.

indicates the presence of expanding motions that are not suitable to flat face-on structures.

3) The optical and radio continuum emission distribution inside the nebula (see below), which resembles a filled sphere of ionized gas inside the IR emission.

In a qualitative manner, the morphology of Gum 31 (strong IR emission towards the border of the nebula and weak emission at the center) depicts the typical emission distribution of optically thin emission of a bubble, scaling with the line-of-sight path length towards the edge of the shell. This effect is known as "limb brightening" (see Fig. 2). The weak 870 μm emission at the center may be due to gas/dust from the front face of the bubble with column density that is too low to be clearly detected. The limb brightening effect has been used to explain the shape of many IR ring bubbles (e.g. Watson et al. 2008; Deharveng et al. 2010), and could also be used to explain the spatial distribution of candidate YSOs observed in the nebula, which seems to be more crowded at the edge of the bubble (see Fig. 8 of OPG13). High-resolution molecular observations of the whole nebula would be useful to confirm the bubble morphology proposed above for Gum 31.

In the upper panel of Fig. 3 we show the 870 μm emission (white contours) and the SUMSS 843 MHz radio continuum emission (cyan contours) overlaid onto the optical (DSSR2) image (in green) and infrared (IRAC-GLIMPSE) 8 μm emission (in red). At 8 μm, most of the emission originates in strong features of PAH molecules, which are considered to be good tracers of warm UV-irradiated photodissociation regions (PDR; Hollenbach & Tielens 1997). Since these complex molecules are destroyed inside the ionized gas of an HII region (Cesarsky et al. 1996; Povich et al. 2007; Lebouteiller et al. 2007), they indicate the limits of the ionization front and delineate the boundaries of the bubble nebula. The 870 μm emission follows the 8 μm emission distribution, which is bright in the western and southern regions of Gum 31. The 843 MHz radio continuum and optical emissions appear mostly confined within the IR bubble. Three emission peaks can be noticed in the radio continuum emission at RA, Dec(J2000) = $10^{h}37^{m}24^{s}$, $-58°39'57''$, RA, Dec(J2000) = $10^{h}37^{m}18^{s}$, $-58°34'50''$, and RA, Dec(J2000) $\approx$ $10^{h}36^{m}59^{s}$, $-58°35'20''$. The last one is elongated and coincident with strong 870 μm emission, which strongly suggests that dense cold dust and molecular gas have been compressed and collected behind the ionization front due to the expansion of the HII region. The other two radio continuum maxima are coincident with strong optical emission.

The presence of intense emission in optical, 8 μm, radio continuum, and 870 μm emission, to the west of the powering stars speaks in favor of the existence of a PDR at the interface between the ionized and molecular gas, as suggested by CNAV08. On the other hand, the strong radio continuum, optical, and IR emission observed in the western region of the bubble in comparison with the emission at the eastern and northeastern edges suggests that the HII region is expanding anisotropically, probably due to the lack of dense molecular gas at the eastern and northeastern edges of the bubble.

As can be seen in Fig. 3, a considerable deficit in the 8 μm and 870 μm emission is visible around RA, Dec(J2000) $\approx$ $10^{h}36^{m}50^{s}$, $-58°43'20''$, coincident with a lack of CO emission (CNAV08) and with the presence of some weak Hα and radio continuum emission located outside the border of the PDR. In Sect. 3.3 (Fig. 6) we show that this region is correlated with a significant dust temperature enhancement. This could indicate that UV photons from the nebula could be leaking into the ISM through a discontinuity in the PDR. Two other interesting features can be noticed when comparing the 8 μm and 870 μm emissions at RA, Dec(J2000) $\approx$ $10^{h}37^{m}03^{s}$, $-58°24'23''$ and RA, Dec(J2000) $\approx$ $10^{h}37^{m}42^{s}$, $-58°27'00''$. The 870 μm structures at these positions (which will be identified in Sect. 3.2 as clumps 8, 18, 19, and 35) appear projected onto deep spots of absorption at 8 μm emission, a typical feature of the so-called infrared dark clouds (IRDCs; Egan et al. 1998; Rathborne et al. 2006).

In the lower panel of Fig. 3 we show the 870 μm emission (green contours) overlaid on the three-color image of the *Herschel* 70 μm (in blue), 250 μm (in green), and 500 μm (in red) emissions. The 250 μm and 500 μm emission follow the 870 μm emission, although they seem to be a bit more extended. This means that the *Herschel* emission at high wavelengths is still good tracer of cold dust in Gum 31. A comparison between the 870 μm emission and the 250 μm and 500 μm emissions in the southern part of the nebula (Dec $\sim -58°46'00''$) shows that the area mapped with LABOCA almost covers the whole cold dust in the region. Since the emission at 250 μm and 500 μm is extremely faint at the eastern and northeastern regions of Gum 31, where no CO(1−0) emission was detected either (Yonekura et al. 2005, CNAV08), we infer that there is little dense molecular gas/dust in the unmapped area of the HII region (see Sect. 3.3.4). This may indicate that Gum 31 has evolved in an inhomogeneous medium, with more material and higher densities towards its western edge. The 70 μm emission, which traces warm dust, is very intense along a very thin lane at the inner border of the PDR. This is a common feature observed in many Galactic IR bubbles (e.g., Anderson et al. 2012). The 70 μm emission is coincident with strong 870 μm emission in the southern region of the bubble, where the emission at 8 μm, 250 μm, and 500 μm is also intense; this gives an idea of the complex nebula morphology.

3.2. Identification of dust clumps at 870 μm

As mentioned in Sect. 3.1, Fig. 1 shows that the dust emission is not uniformly distributed, and several condensations can be distinguished in the whole structure. These condensations must be identified and their physical properties must be estimated if a study of the physical properties of the cold dust and molecular gas in the whole bubble nebula is to be carried out. Different terminologies have been used in recent years to describe the substructure of a molecular cloud. A hierarchical classification was proposed by Blitz (1993) for structures of different scales in the interstellar medium: clouds, clumps, and cores. Clouds have masses $>10^4$ $M_\odot$, and cores (regions where single stars or binary systems might be formed) have masses <10 $M_\odot$ and sizes <0.1 pc. Clumps are then structures with intermediate

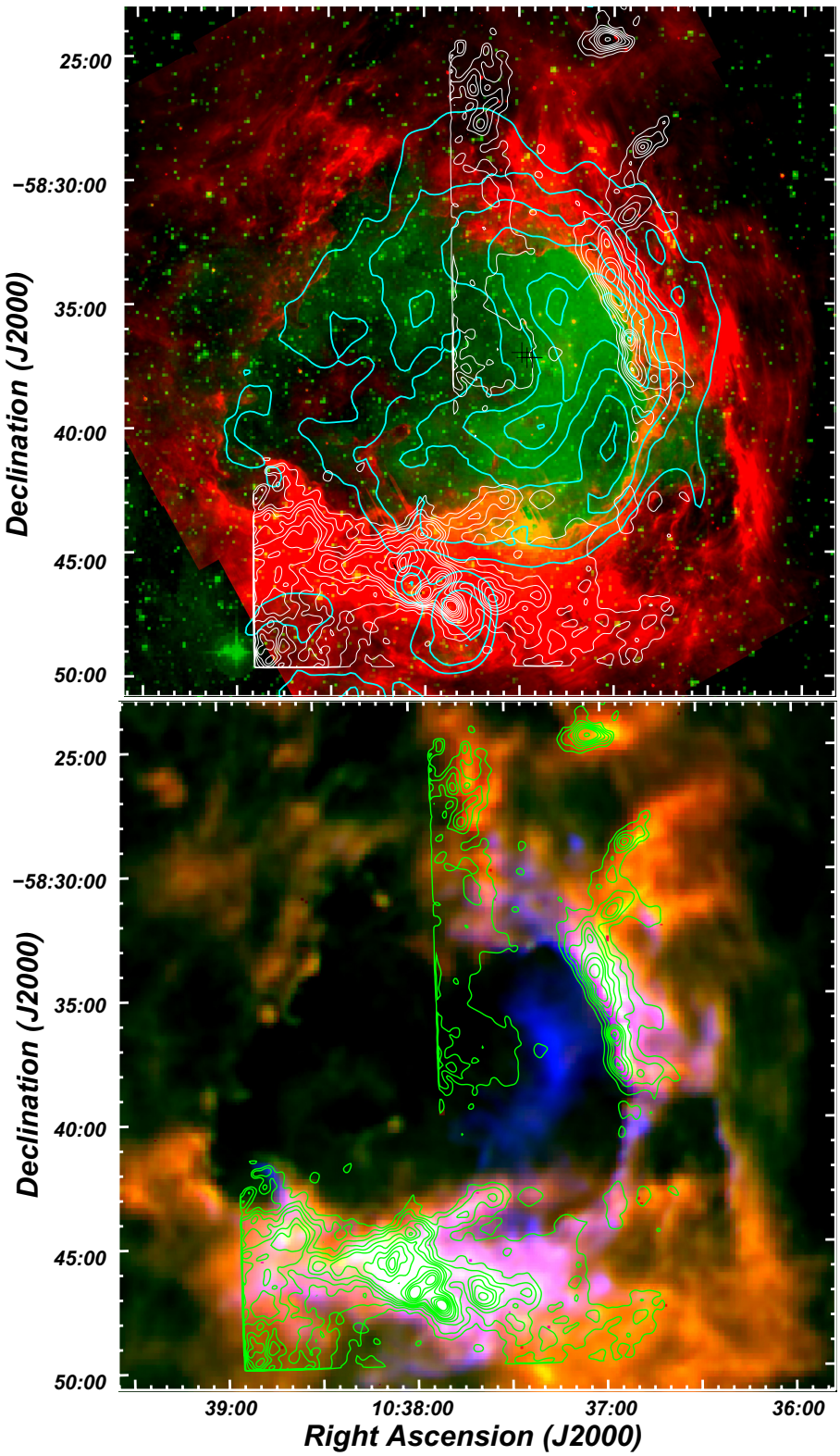

Fig. 3. *Upper panel*: composite image of Gum 31 and its environs. The IRAC-GLIMPSE emission at 8.0 μm is shown in red, while green indicates the DSSR2 optical emission (red plate). White contours show the 870 μm emission while cyan contours shows the radio continuum emission at 843 MHz. Black crosses at the center show the position of stars HD 92206A, B, and C. *Lower panel*: composite image of the 870 μm dust continuum emission (green contours) overlaid onto the *Herschel* 70 μm (blue), 250 μm (green), and 500 μm (red) emissions. The contours corresponding to the 870 μm emission in both panels are the same as in Fig. 1.

masses and sizes from which stellar clusters can be formed. A similar classification was proposed by Bergin & Tafalla (2007) and Williams et al. (2000) designating individual overdensities inside a molecular cloud, which can be identified by different automated algorithms, as clumps. Given the characteristics mentioned above and the physical properties derived for the condensations distinguished in the 870 μm emission, we will hereafter refer to these structures as "clumps".

We have identified the dust clumps in Gum 31 in a systematic way with the commonly used `Gaussclumps` algorithm (Stutzki & Guesten 1990; Kramer et al. 1998), a task included in the GILDAS[8] package. Although `Gaussclumps` was originally written to work on a three-dimensional data cube, it can be modified to be applied to continuum images without modification of the code by adding two two-dimensional empty planes

[8] http://www.iram.fr/IRAMFR/GILDAS

to the original continuum image mimicking a three-dimensional datacube (see Motte et al. 2003). `Gaussclumps` uses a least-squares fitting procedure to decompose the image/cube into a series of Gaussian-shaped clumps by iteratively substracting fitted clumps. The algorithm identifies the position, peak flux density, full width at half maximum (FWHM), and position angle of the fitted sources. As suggested by Kramer et al. (1998), the "stiffness" parameters that control the fitting were all set to 1. The peak flux density threshold was set to 4σ. To avoid false detections, we trimmed the noisy borders of the image and added a wedge of null values to force `Gaussclumps` to identify clumps inside the image. To identify genuine clumps we imposed that the deconvolved size of the clumps should be larger than 50% of the HPBW size (i.e., $R_{\rm D} > HPBW/2$, or 0.12 pc at a distance of 2.5 kpc). As a result, 41 clumps were identified in the 870 μm emission image.

In Table 1 we present all the clumps identified with `Gaussclumps`. The identification number of the clumps and their coordinates are indicated in Cols. 1 and 2, respectively. The spatial location, numerical identification, size, and orientation derived for each clump are depicted in Fig. 4. As can be seen from this figure, most of clumps satisfy a convincing visual identification. In Col. 11 of Table 1 we indicate the HCO^+ clumps reported by Barnes et al. (2011) that are projected over the corresponding 870 μm clump. Clumps 1, 6, and 3 were reported by Vazzano et al. (2014), labeled in that work as D1, D2, and D3, respectively (see Fig. 7 of that work).

In Sect. 3.1, we pointed out that clumps 8, 18, 19, and 35 appear projected onto deep spots of absorption at 8 μm emission, which suggests that these clumps could be foreground dense objects. These clumps, very bright at 250 μm and 500 μm but not emitters at 70 μm, appear quite isolated and projected slightly farther from the nebula, casting some doubts on their association with the rest of the clumps and their interaction with the ionization front. Since their velocities are in agreement with the rest of the clumps (Barnes et al. 2011) we infer that these clumps could be remnants of the parental cloud that remains undisturbed by the expansion of the nebula.

With the aim of studying the northeastern region of the Gum 31 nebula, which was not observed with LABOCA (see Sect. 3.1), we make use of *Herschel* images at 250 μm since the emission at this wavelength is still a good tracer of cold dust. The identified clumps are presented in the lower part of Table 1. The number identification of the clumps are continued from those identified at 870 μm. The spatial location, numerical identification, size, and orientation derived for each clump are depicted in Fig. 5. We have rejected two clumps from the sample around the position RA, Dec(J2000) $\approx 10^{\rm h}38^{\rm m}35^{\rm s}$, $-58°42'30''$, since they are likely the 250 μm counterparts of clumps 9, 24, and 28. We note that clumps 49, 57, and 60 are projected over the center of the nebula and show a good spatial correlation with regions of optical absorption (see Fig. 3), which could indicate that these clumps are placed in front of the nebula. These clumps have low column and volume densities and could be related with the faint IR emision at the center of the nebula, giving more support to the bubble morphology proposed earlier for Gum 31.

We are cautious about the clump identification described above, an about the physical properties (see next section), since the IR nebula was proposed to be the result of a projection of a three-dimensional bubble onto a two-dimensional plane. This problem, however, does not only concern the case of Gum 31, but should be also addressed in many other molecular studies of Galactic bubble nebulae, where different molecular clumps (or condensations) have been studied.

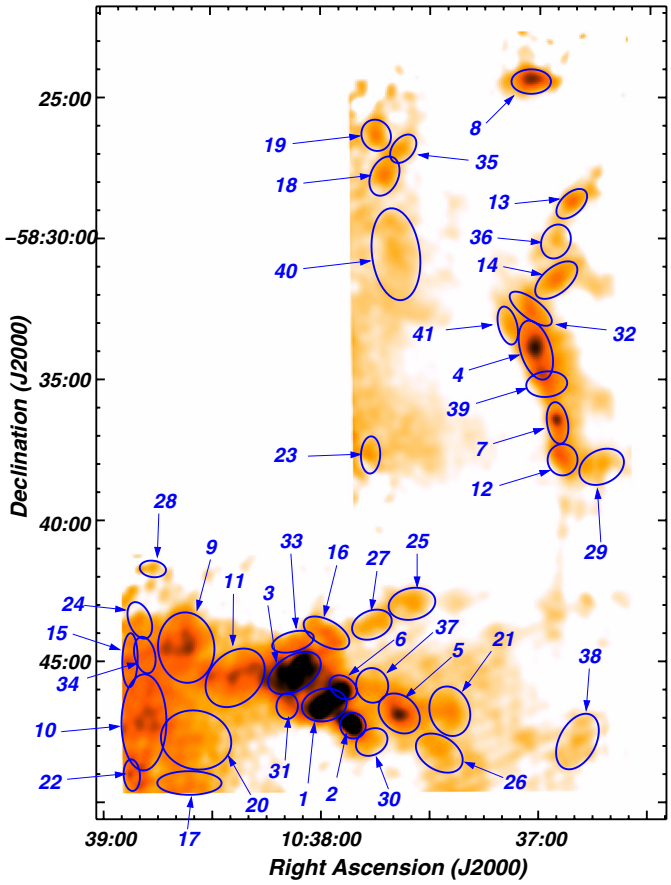

Fig. 4. Clumps identified with `Gaussclumps` in the 870 μm emission image.

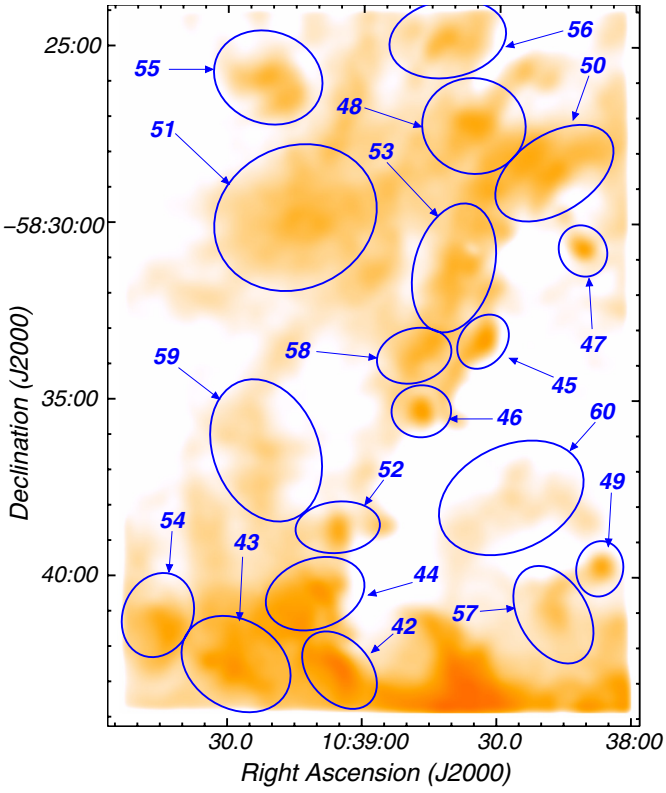

Fig. 5. Clumps identified with `Gaussclumps` algorithm in the 250 μm emission image, over the uncovered region in 870 μm emission.

Table 1. Properties of identified clumps around the bubble HII region Gum 31.

Clump number	RA, Dec$_{J2000}$ (^{hms}, $^{\circ}\,'\,''$)	I_{peak} ($\frac{Jy}{beam}$)	S_ν (Jy)	$\theta_{maj} \times \theta_{min}$ ($'' \times ''$)	R_D (pc)	M_{tot} ($M_\odot$)	n (cm^{-3})	N_{H_2} (10^{22} cm^{-2})	T_{dust} (K)	HCO$^+$ (BYF†)
1	10 37 59, –58 46 34	1.76	23.41	86.8 × 61.1	0.42	2050	93 500	10.4	25	77b
2	10 37 51, –58 47 18	1.71	8.21	45.7 × 41.8	0.23	770	203 800	10.9	24	77a
3	10 38 07, –58 45 26	1.59	30.26	113.9 × 66.5	0.51	2800	72 300	9.9	24	77c
4	10 37 01, –58 33 59	0.96	16.62	120.3 × 57.5	0.48	1450	43 800	5.6	25	70a
5	10 37 38, –58 46 52	0.92	13.51	87.5 × 66.7	0.44	1130	43 900	5.2	26	77d
6	10 37 54, –58 45 57	0.93	4.65	53.5 × 37.2	0.23	410	103 400	5.5	25	77b
7	10 36 55, –58 36 34	0.83	6.11	79.4 × 36.8	0.29	530	70 700	4.9	25	70b
8	10 37 02, –58 24 27	0.87	7.21	74.6 × 44.1	0.32	820	84 400	6.7	21	67
9	10 38 37, –58 44 32	0.79	28.03	130.1 × 108.7	0.71	2430	23 300	4.6	25	
10	10 38 49, –58 47 10	0.76	32.98	194.8 × 88.3	0.78	2640	18 900	4.1	26	
11	10 38 24, –58 45 36	0.73	18.59	132.8 × 76.1	0.59	1640	26 900	4.4	25	
12	10 36 54, –58 37 52	0.56	4.52	56.7 × 56.1	0.31	390	40 600	3.2	25	70b
13	10 36 51, –58 28 47	0.56	3.65	69.3 × 37.1	0.27	370	60 800	3.9	22	66
14	10 36 56, –58 31 30	0.52	6.10	96.8 × 48.2	0.39	580	33 600	3.3	23	69
15	10 38 53, –58 44 58	0.54	3.56	105.0 × 24.8	0.23	290	76 200	3.0	26	
16	10 37 58, –58 44 01	0.51	5.84	97.4 × 46.2	0.38	480	29 600	2.9	26	
17	10 38 36, –58 49 20	0.51	6.95	127.8 × 42.3	0.41	540	26 100	2.7	27	
18	10 37 43, –58 27 49	0.48	4.93	77.8 × 52.7	0.36	470	32 500	3.1	23	72
19	10 37 45, –58 26 22	0.48	3.75	58.2 × 53.6	0.31	370	40 600	3.2	23	72
20	10 38 34, –58 47 48	0.48	16.91	130.1 × 106.5	0.70	1290	12 800	2.5	28	
21	10 37 25, –58 46 48	0.46	8.71	97.5 × 77.4	0.51	700	17 900	2.5	27	
22	10 38 52, –58 49 03	0.50	1.94	57.2 × 26.8	0.18	150	77 100	2.6	27	
23	10 37 46, –58 37 42	0.40	2.30	69.2 × 33.2	0.25	140	30 100	1.7	32	
24	10 38 50, –58 43 33	0.38	2.68	71.5 × 39.1	0.29	200	27 900	1.9	28	
25	10 37 35, –58 42 59	0.36	4.86	91.1 × 58.9	0.42	390	17 400	1.9	27	
26	10 37 27, –58 48 17	0.34	5.48	99.0 × 63.7	0.46	470	16 300	2.0	25	
27	10 37 46, –58 43 43	0.34	3.44	78.1 × 51.8	0.36	270	19 100	1.8	27	
28	10 38 46, –58 41 44	0.33	1.05	46.5 × 26.8	0.16	70	52 700	1.5	28	
29	10 36 43, –58 38 07	0.33	4.79	90.5 × 63.0	0.44	390	15 600	1.8	26	
30	10 37 46, –58 47 53	0.34	2.37	61.3 × 44.5	0.29	170	23 500	1.6	29	
31	10 38 09, –58 46 37	0.34	1.47	44.9 × 38.0	0.21	120	38 600	1.8	27	
32	10 37 02, –58 32 31	0.32	2.68	98.3 × 33.7	0.30	240	27 900	1.9	24	
33	10 38 08, –58 44 20	0.35	2.35	83.4 × 32.2	0.27	180	30 900	1.8	27	
34	10 38 49, –58 44 47	0.33	2.09	69.1 × 36.1	0.27	170	30 200	1.9	26	
35	10 37 37, –58 26 50	0.31	1.74	59.0 × 37.4	0.25	160	34 700	2.0	24	72
36	10 36 56, –58 30 07	0.31	2.69	64.8 × 53.1	0.33	240	22 100	1.9	25	
37	10 37 46, –58 45 53	0.33	3.22	64.1 × 60.4	0.35	240	17 700	1.6	28	
38	10 36 49, –58 47 51	0.29	6.04	117.7 × 70.0	0.53	520	11 700	1.7	25	
39	10 36 58, –58 35 11	0.30	2.75	78.0 × 46.2	0.34	220	19 200	1.6	28	
40	10 37 39, –58 30 35	0.28	12.56	187.0 × 94.5	0.79	990	6800	1.5	27	
41	10 37 09, –58 33 07	0.29	1.73	72.8 × 32.0	0.25	130	27 600	1.5	28	
42	10 39 05, –58 42 40	8.94	329.38	147.3 × 80.9	0.65	550	6800	1.2	25	
43	10 39 28, –58 42 36	7.31	464.92	162.3 × 126.9	0.86	810	4400	1.1	24	
44	10 39 10, –58 40 25	6.91	270.21	127.7 × 99.2	0.67	470	5300	1.0	24	
45	10 38 34, –58 33 21	6.21	153.44	101.8 × 78.5	0.53	240	5600	0.8	25	
46	10 38 47, –58 35 20	6.04	170.64	103.5 × 88.4	0.56	270	5100	0.8	25	
47	10 38 11, –58 30 46	5.69	128.66	90.4 × 81.0	0.50	200	5300	0.7	25	
48	10 38 36, –58 27 15	5.94	394.71	156.4 × 137.6	0.88	680	3400	0.8	24	
49	10 38 07, –58 39 45	5.45	129.48	94.8 × 81.1	0.52	180	4400	0.6	27	
50	10 38 18, –58 28 34	5.59	397.16	208.4 × 110.5	0.91	520	2400	0.6	27	
51	10 39 15, –58 29 52	5.44	846.49	242.6 × 207.4	1.35	1390	1900	0.7	25	
52	10 39 06, –58 38 37	5.28	149.84	120.4 × 76.3	0.56	230	4300	0.7	26	
53	10 38 40, –58 31 16	5.29	368.83	178.7 × 126.2	0.90	510	2400	0.6	27	
54	10 39 45, –58 41 16	5.33	292.23	147.5 × 120.4	0.79	520	3450	0.8	24	
55	10 39 21, –58 25 54	5.20	312.22	160.3 × 121.3	0.83	600	3500	0.8	23	
56	10 38 42, –58 24 47	5.09	285.67	184.5 × 184.5	0.80	610	4000	0.9	23	
57	10 38 17, –58 41 04	4.79	290.35	176.9 × 111.0	0.84	360	2100	0.5	28	
58	10 38 49, –58 33 44	4.69	175.54	131.5 × 92.0	0.65	270	3300	0.6	25	
59	10 39 22, –58 36 27	4.23	597.59	251.0 × 182.3	1.29	890	1400	0.5	26	
60	10 38 27, –58 37 46	3.75	542.53	263.4 × 177.8	1.30	670	1100	0.4	28	

Notes. Clumps 1 to 41 were identified at 870 μm while clumps 42 to 60 at 250 μm. $^{(\dagger)}$ From Table 4 and Fig. 34 of Barnes et al. (2011).

3.3. Physical properties of the clumps

3.3.1. Temperature

In many works, it is assumed that (sub)millimeter clumps/clouds would have a common temperature (e.g., Mookerjea et al. 2004; Kirk et al. 2006; López et al. 2011). This is a logical assumption in the case of isolated clouds, athough it is not valid for regions like Gum 31, where different parts of the nebula are affected by different levels of radiation. We have used the 70 μm and 160 μm *Herschel* images to obtain the dust temperature of the clumps and of the whole Gum 31. To construct the flux-ratio map, the 70 μm map was smoothed down to the angular resolution of the 160 μm map. We divided the intensities of the maps by the recommended color-correction factors described by Bernard et al. (2010): 1.05 for the 70 μm and 1.29 for the 160 μm, values derived from a comparison with Planck data. The zero-level of the PACS archive data is unknown, which may cause problems for deriving the background emission in each map. Here we adopted the background levels of 0.0023 Jy/px for 70 μm and 0.005 Jy/px for 160 μm found by Preibisch et al. (2012). Then, the color-temperature map was constructed as the inverse function of the ratio map of Herschel 70 and 160 μm color- and background-corrected maps, i.e., $T_{\rm c} = f_{(T)}^{-1}$ (see details in Preibisch et al. 2012).

Assuming a dust emissivity following a power law $\kappa_\nu \propto \nu^\beta$, being β the spectral index of the thermal dust emission, in the optically thin thermal dust emission regime $f_{(T)}$ has the parametric form:

$$f_{(T)} = \frac{S_{70}}{S_{160}} = \frac{B(70,T)}{B(160,T)} \left(\frac{70}{160}\right)^{\beta}, \quad (1)$$

where $B(70,T)$ and $B(160,T)$ are the blackbody *Planck* function for a temperature T at the frequencies 70 μm and 160 μm, respectively. The pixel-to-pixel temperature was calculated assuming a typical value $\beta = 2$ (see Preibisch et al. 2012 and references therein) on the whole Gum 31 region. The uncertainty in derived dust temperatures using this method was estimated to be about ~10−15% (Preibisch et al. 2012).

In Fig. 6 we show the color-temperature map obtained using the method explained above. The map shows a good correspondence with that obtained in Preibisch et al. (2012) and Ohlendorf et al. (2013), indicating temperatures $\lesssim$28 K for clumps lying at the outer border of the bubble, while clumps projected over the inner region of the bubble (clumps 23, 28, and 60) show temperatures $\gtrsim$28 K, with the exception of clump 49. Inside the bubble, close to the position of the stars of NGC 3324 (where no 870 μm emission is detected), temperatures are above 35 K. The lowest derived dust temperature is 21 K, corresponding to clump 8. The most remarkable feature in Fig. 6 is the excellent morphological correspondence of the 870 μm emission with darker regions in the temperature map, which confirms that we are dealing with the coldest and the densest molecular gas and dust that were collected behind the ionization front of the HII region bubble.

Temperatures of the clumps ($T_{\rm dust}$, Col. 10 in Table 1) were simply estimated by positioning the center of the fitted Gaussian on the color temperature map.

3.3.2. Mass

The total (H_2 + dust) mass of the clumps ($M_{\rm tot}$, Col. 7 in Table 1) was calculated from their integrated 870 μm emission (S_{870}, Col. 4 in Table 1), assuming that the emission is optically thin, using the equation of Hildebrand (1983),

$$M_{\rm (tot)} = R\, \frac{S_{870}\, d^2}{\kappa_{870}\, B_{870}(T_{\rm dust})} \quad (2)$$

where R is the gas-to-dust ratio, d is the distance (adopted as 2.5 kpc), κ_{870} is the dust opacity per unit mass at 870 μm assumed to be 1.0 cm^2 g^{-1} (estimated for dust grains with thin ice mantles in cold clumps; Ossenkopf & Henning 1994), and $B_{870}(T_{\rm dust})$ is the Planck function for a temperature $T_{\rm dust}$. For the case of the clumps detected in the *Herschel* 250 μm emission, we used a dust opacity $\kappa_{250} = 12.1$ cm^2 g^{-1}, which is consistent with $\kappa_{870} = 1.0$ cm^2 g^{-1} (assuming $\kappa_\nu \propto \nu^2$). Adopting $R = 186$ (Jenkins 2004; Draine et al. 2007; Beuther et al. 2011), derived masses are in the range from 70 $M_\odot$ to 2800 $M_\odot$ and the total mass is ~37 600 $M_\odot$. This is a lower limit for the total mass in the nebula, since substantial 870 μm emission lying outside the boundaries of the clumps was not taken into account (see Fig. 4). In addition, some of the 870 μm emission towards the center of the nebula (see Sect. 3.1) was probably not detected. We estimate a total mass uncertainty of about 50−60% arising mostly from a conservative distance uncertainty of ~20% and a dust temperature uncertainty of 15%.

3.3.3. Size

The effective deconvolved radius of the clumps ($R_{\rm D}$, Col. 7 in Table 1) was calculated as

$$R_{\rm D} = \sqrt{\frac{\theta_{\rm maj}}{2} \times \frac{\theta_{\rm min}}{2}}, \quad (3)$$

where $\theta_{\rm maj}$ and $\theta_{\rm min}$ are the major and minor deconvolved FWHM of the clump (Col. 5 in Table 1). These values were obtained as

$$\theta_{\rm maj} = \sqrt{{\rm d}x^2 - \theta^2_{\rm HPBW}} \;\text{ and }\; \theta_{\rm min} = \sqrt{{\rm d}y^2 - \theta^2_{\rm HPBW}}\,, \quad (4)$$

being dx and dy the major and minor FWHM sizes derived by the `Gaussclumps` algorithm, and $\theta_{\rm HPBW}$ the final resolution of the image (20″ for 870 μm and 18″ for 250 μm). Clump radii are found to lie between 11.″1 and 65.″2 (0.16 pc and 0.79 pc, respectively, at a distance of 2.5 kpc) for 870 μm, while for 250 μm clump radii are between 41.″3 to 111.″4 (0.5 pc to 1.35 pc at a distance of 2.5 kpc). The difference could be that the emission at 250 μm may be tracing warmer and less dense dust than the 870 μm emission making its emission more extended (see Fig. 3). This could affect the determination of the volume densities of the clumps, which are slightly lower than those determined from the 870 μm emission (see next section).

3.3.4. Densities

The average volume density of each clump (n, Col. 8 in Table 1) was derived, assuming a spherical geometry, as

$$n = \frac{M_{\rm (tot)}}{4/3\, \pi\, R_{\rm D}^3\, \mu\, m_{\rm H}} \quad (5)$$

where μ is the mean molecular weight (assumed to be 2.8 after allowance of a relative helium abundance of 25% by mass), and $m_{\rm H}$ is the mass of the hydrogen atom. Volume densities of the clumps are between 1.1×10^3 cm^{-3} and 2.03×10^5 cm^{-3}. The average density of the sample is 2.9×10^4 cm^{-3}.

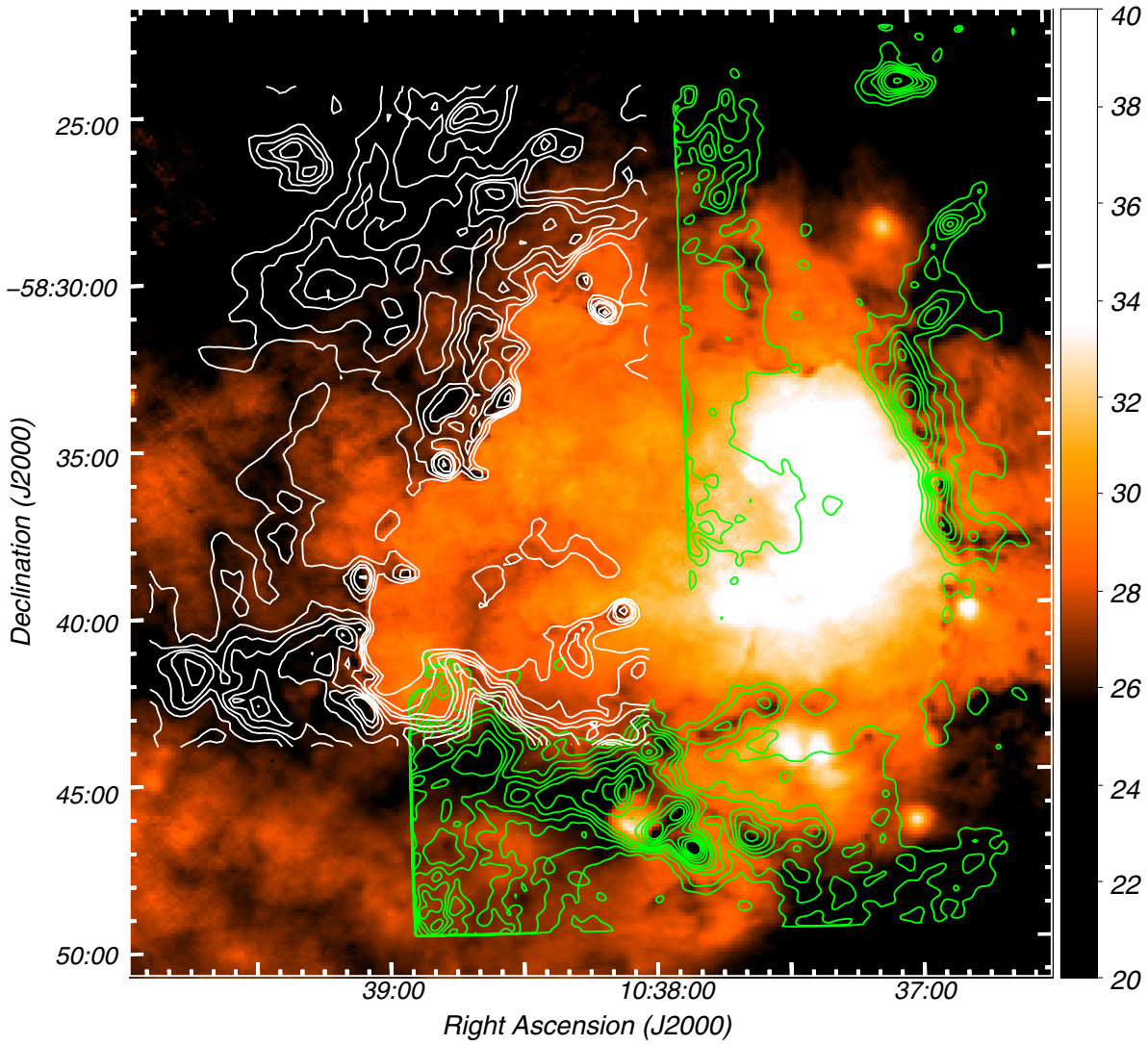

Fig. 6. Dust temperature map (in color scale) derived from *Herschel* emission at 70 and 160 μm. The color-temperature scale is on the right. The 870 μm emission is shown in green contours and the 250 μm emission is shown in white contours. The 870 μm contours are the same as in Fig. 1 and the 250 μm contours go from 410 mJy beam^{-1} (~4σ) to 590 mJy beam^{-1} in steps of 50 mJy beam^{-1}, and from 700 mJy beam^{-1} in steps of 100 mJy beam^{-1}.

The beam-averaged column density of the clumps (N_{H_2}, Col. 9 in Table 1) was calculated using

$$N_{H_2} = R \frac{I_{peak}}{\Omega_{beam}\, \kappa_{870}\, \mu\, m_H\, B_{870}(T_{dust})} \quad (6)$$

(Hildebrand 1983), where I_{peak} is the 870 μm emission peak intensity (Col. 3 in Table 1) and Ω_{beam} is the beam solid angle ($\pi\ \theta^2_{HPBW}/4\ln(2)$). As we did when determining the mass, we assumed $R = 186$. Considering a lower limit for the solid angle corresponding to the HPBW size, an intensity peak limit of 3σ (150 mJy beam^{-1} for 870 μm, and 400 mJy beam^{-1} for 250 μm), and a maximum dust temperature for the clumps of 32 K (see Table 1), the minimum beam-averaged column densities detectable at 870 μm and 250 μm are 0.63×10^{22} cm^{-2} and 0.32×10^{22} cm^{-2}, respectively.

Column densities derived for all the identified clumps are between 0.38×10^{22} cm^{-2} and 10.85×10^{22} cm^{-2}. The average column density of the sample is $\sim 2.4 \times 10^{22}$ cm^{-2}, almost twice the value obtained by CNAV08 for the molecular shell associated with Gum 31. This is not surprising given that we are probing the molecular gas intimately associated with the ionization front of the HII region, which is more affected by the expansion of the nebula. We keep in mind that this difference could also be due to different angular resolutions and abundance variations. We note that volume densities of the 870 μm clumps are, on average, larger than those of 250 μm clumps by a factor of ~10. The same occurs with column densities, which are larger by a factor of ~5. A possible explanation for this difference is an evolution of the HII region in an inhomogeneous cloud. The faint 8 μm, 250 μm, and 500 μm emission towards the eastern and northeastern regions of Gum 31 supports this scenario (see Sect. 3.1). On the other hand, as suggested in Sect. 3.3.3, the 250 μm emission could be tracing warmer and less dense dust than the 870 μm emission. A combination of both factors is also possible.

The physical properties derived for the dust clumps in Gum 31 (radius, density and mass) are comparable to those found in IR continuum clumps detected in other Galactic star-forming regions (e.g., Mookerjea et al. 2004; López et al. 2011; Beuther et al. 2011).

3.4. Clump mass distribution

Using the mass obtained for each clump, we derived the clump mass distribution (CMD) in the Gum 31 region. The CMD is

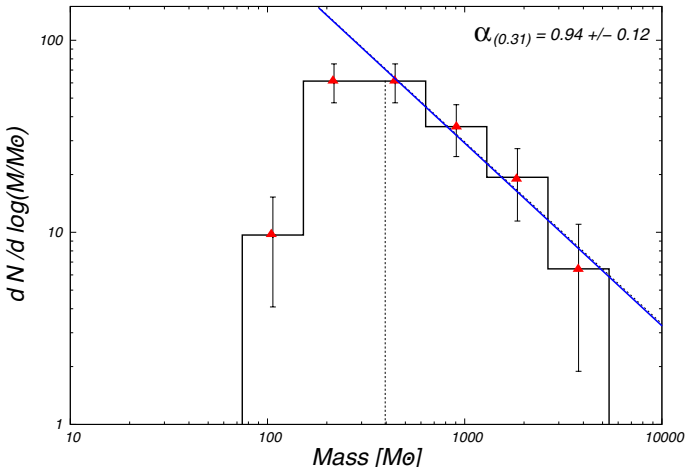

Fig. 7. Example of a CMD for $\Delta\log(M/M_\odot) = 0.31$. Red triangles represent the central mass of each bin and error bars represent the standard deviation of a Poisson distribution ($\sqrt{\Delta N}$). Blue lines represent the best fit above the 400 $M_\odot$ limit (dotted vertical line).

plotted as $dN/d\log(M/M_\odot)$ versus mass. The first term is approximated as the number of clumps in each mass interval (N) and the second is approximated by the logarithmic mass interval, $\Delta\log(M/M_\odot)$. The error was determined considering only the statistical Poisson uncertainty, $\sqrt{\Delta N}$. We fitted the histograms with a power law of the form $dN/d\log(M/M_\odot) \propto M^{-\alpha}$, where α is the spectral mass index. A CMD can also be plotted as $dN/d(M/M_\odot)$, which has a power-law dependence $dN/d(M/M_\odot) \propto M^{-\Gamma}$, where $\Gamma = \alpha + 1$.

To overcome fitting artifacts due to different bin sizes ($\Delta\log(M/M_\odot)$), we derived spectral indexes for different bin sizes, ranging from 0.25 to 0.45 in steps of 0.01. For each logarithmic bin size we fitted the corresponding spectral mass index. In all the cases, a turnover in the distribution can be seen at bins between 300 $M_\odot$ and 500 $M_\odot$, which is likely caused by the low-mass incompleteness. To make sure that the fit is not affected by incompleteness effects at lower masses, we use a lower cut-off of 400 $M_\odot$ for the fit. In Fig. 7 we show an example of a CMD derived for $\Delta\log(M/M_\odot) = 0.31$. The procedure resulted in 21 fits, obtaining spectral indexes α in the range 0.44−1.35, with a final weighted mean spectral index $\alpha = 0.93 \pm 0.28$.

Although making a comparison of the spectral mass indexes is a complex task owing to the many assumptions authors made, especially when extracting clumps and deriving their masses, the average spectral mass index derived for the dust clumps in Gum 31 is comparable to others derived for molecular clouds from dust continuum (e.g., Mookerjea et al. 2004; López et al. 2011; Beuther et al. 2011; Miettinen 2012) and from molecular line CO observations (e.g., Blitz 1993; Kramer et al. 1998; Simon et al. 2001, 2006; Heyer et al. 2001; Wong et al. 2008).

The slope of a CMD is usually compared to that of the initial stellar mass function (IMF; Salpeter 1955) as a way to asses a direct relation clump-star (Motte et al. 1998; Lada et al. 2007; López et al. 2011). Equal slopes would indicate that clumps form stars directly. The weighted average slope derived for Gum 31 is shallower than Salpeter's value ($\alpha = 1.35$ or $\Gamma = 2.35$) and other indexes between 2.1 and 2.5 in the upper mass regime (above ∼1 $M_\odot$; Kroupa 2001; André et al. 2010) implying that the clumps are not direct progenitors of individual stars. This means that other processes, such as fragmentation (mainly of the most massive clumps) are necessary to determine the initial stellar masses. We keep in mind, however, that observations with higher spatial resolution, resolving core structures of ∼0.1 pc in size, could result in a spectral index of ∼2.35 (e.g., Motte et al. 1998). In this line, we emphasize that the radii of the clumps are between 0.16 pc and as large as 1.35 pc in size (most of them having sizes above 0.4 pc), which are about the size of star-forming regions, rather than individual star-forming cores (typically between 0.01 pc and 0.1 pc in size). Smaller clumps (or cores), may not be correctly separated with the resolution of the LABOCA data, although this is just speculation. Since these hypothetical smaller cores cannot be identified in *Herschel* images, higher spatial resolution images (*HPBW* < 8″, equivalent to sizes <0.1 pc at a distance of 2.5 kpc) of the whole nebula would be useful to shed some light on this issue.

3.5. Star formation evidence

According to Lada & Lada (2003) and Motte et al. (2003) the radius and mass required to form stellar clusters are about 0.5 pc to 1 pc and 100 $M_\odot$ to 1000 $M_\odot$, respectively, which are comparable to those obtained with `Gaussclumps` in Gum 31. The clumps identified with `Gaussclumps` in the 870 μm emission are then good candidates to form clusters of stars, rather than individual stars. As pointed out in Sect.1, an exhaustive search of YSO candidates was carried out by OPG13 using high sensitivity and high spatial resolution IR data. Although some contamination from the fore- and background sources is present, OPG13 considered the WISE-selected sample of YSO candidates to be the more reliable, finding 661 candidates (207 Class I and 454 Class II sources) of solar to intermediate mass. Since most of the candidate YSOs detected by OPG13 and CNAV08 appear projected onto the area mapped with LABOCA, and the gas and dust in the eastern and northeastern regions of Gum 31 is much less dense than the southern and western regions, we will concentrate our analysis only on the 870 μm emission.

In Fig. 8 we show the location of the WISE YSO candidates reported by OPG13 that appear projected over the 870 μm emission. The location of the YSOs were cautiously determined using a composite image of 8.0 μm, 4.5 μm, and 3.6 μm emissions as a reference. We have also included the MSX and 2MASS candidate YSOs identified by CNAV08. From a visual inspection of Fig. 8, we can roughly distinguish five clusters of YSO candidates projected onto the submillimeter clumps. Two small compact clusters are approximately centered at RA, Dec(J2000) ≈ $10^h37^m00^s$, −58°34′47″ and RA, Dec(J2000) ≈ $10^h36^m54^s$, −58°37′26″. The first cluster is composed of 10 protostellar members and is projected onto clumps 4, 32, and 39. The second cluster is composed of 13 members and is projected over clumps 7, 12, and 29. In the southern region of the bubble, three clusters can be discerned. The first cluster, approximately centered at RA, Dec(J2000) ≈ $10^h38^m42^s$, −58°45′45″, contains approximately 31 members projected over clumps 9, 10, 11, 15, 20, and 34. The second, located at RA, Dec(J2000) ≈ $10^h38^m02^s$, −58°45′42″, consists of ∼ 29 members projected over clumps 1, 2, 3, 6, 16, 30, and 33, while the third is approximately centered at RA, Dec(J2000) ≈ $10^h37^m13^s$, −58°47′10″, and is composed of approximately 18 members projected only over clump 21.

In Fig. 9 we show the mass-radius relationship for the 41 clumps identified in the 870 μm emission, discriminating between clumps that have candidate YSOs projected inside their limits and clumps without signposts of star formation. For comparison purposes only, we have included the 19 clumps identified in the 250 μm emission.

Kauffmann et al. (2010a,b) and Kauffmann & Pillai (2010) investigated the mass radius relationship of nearby molecular

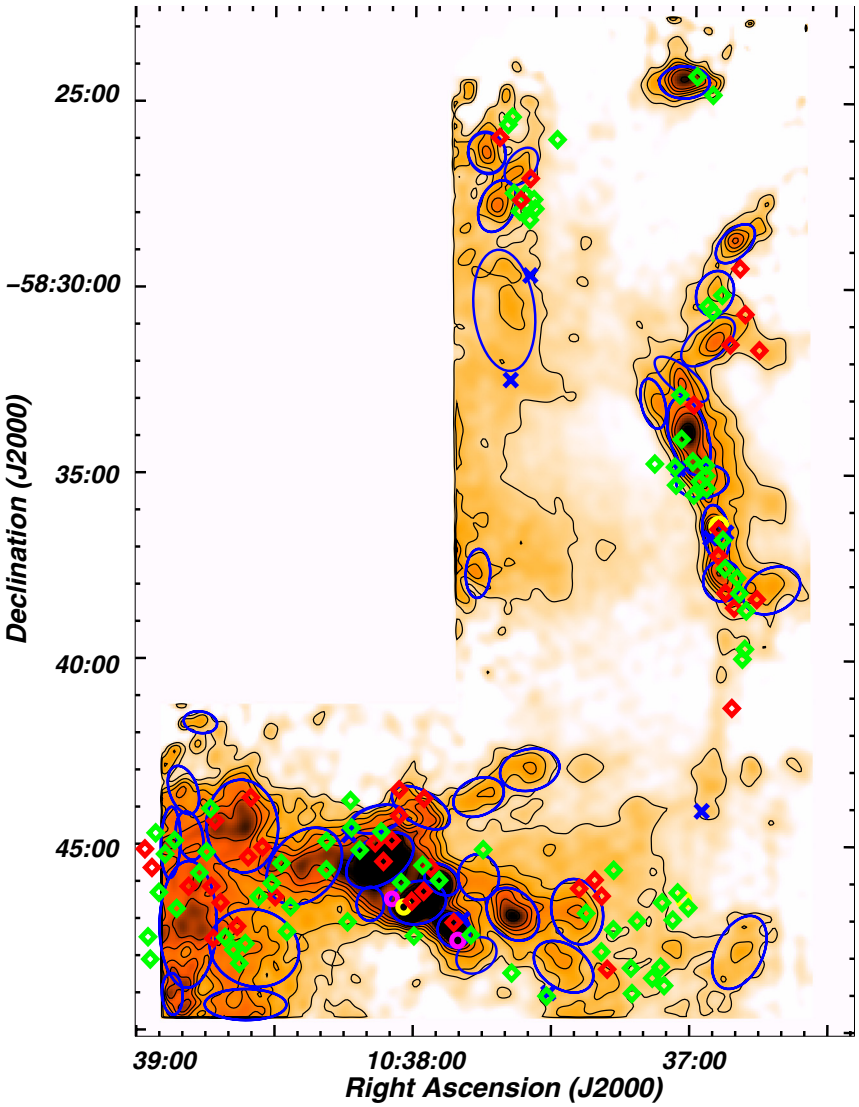

Fig. 8. Candidate YSOs projected over the 870 μm emission. WISE Class I and Class II candidates (OPG13) are marked by red and green diamonds. MSX massive young stellar object (MYSO) and compact HII region candidates (CNAV08) are marked by magenta and yellow circles, respectively, while 2MASS candidate YSOs (CNAV08) are indicated by blue crosses. Molecular clumps identified in Sect. 3 are indicated by blue ellipses.

clouds and found the empirical relationship $M\ [M_\odot] \leq 1972 \times (R_{\rm eff}\ [{\rm pc}])^{1.33}$ as the threshold at which high-mass ($M \sim 10\ M_\odot$) star formation is avoided (hereafter the K&P threshold). We note that when deriving their relationship, Kauffmann et al. reduced the dust opacities of Ossenkopf & Henning (1994) by a factor of 1.5. Since this correction has not been applied here, we have rescaled the relationship given in the original work (cf. Urquhart et al. 2013). The rescaling was also calculated considering the opacities and gas-to-dust ratio used in this work ($\kappa_{870} = 1.0$ cm^2 g^{-1} and $R = 186$; see Sect. 3.3). The K&P threshold is shown in Fig. 9. For the sake of comparison, we also show the empirical mass-size relationship obtained by Urquhart et al. (2013) for intermediate- and high-mass star formation, rescaled to $\kappa_{870} = 1.0$ cm^2 g^{-1} and $R = 186$. The upper and lower red solid lines in Fig. 9 depict the constant surface densities of 1 g cm^{-2} and 0.024 g cm^{-2}, respectively. The surface density of 1 g cm^{-2} (4787 $M_\odot$/pc^2) was advocated by Krumholz & McKee (2008) and McKee & Tan (2003) as criterion to avoid excessive fragmentation and to allow massive star formation. The surface density of 0.024 g cm^{-2} represents the average surface density threshold derived by Lada et al. (2010; 116 $M_\odot$ pc^{-2}) and Heiderman et al. (2010; 129 $M_\odot$ pc^{-2}), for efficient star formation.

As can be seen from Fig. 9, all clumps lie above the lower surface density limit of 0.024 g cm^{-2}. Of the 41 clumps identified in the 870 μm emission, only 15 (37 %) lie above the K&P limit, with 12 clumps (clumps 1, 2, 3, 4, 6, 7, 8, 9, 10, 15, 11, and 20) having candidate YSOs projected inside their limits. Only clumps 5, 13, and 14 are starless clumps. As mentioned in Sect. 3.2, clumps 1 and 3 were found by Vazzano et al. (2014; labeled in their work as D1 and D3, respectively) and were associated by the authors to a dense molecular shell linked to several infrared sources. Clump 1 is coincident with the MSX sources G286.3747-00.2630 and G286.3773-00.2563, which were classified as a compact HII region (CHII) and massive young stellar object (MYSO) candidates, respectively (sources 20 and 21 in CNAV08). Two WISE Class I and Class II candidates identified by OPG13 are projected inside the boundaries of this clump (see Fig. 8). This clump has an HCO^+ counterpart (BYF 77b; Barnes et al. 2011) which confirms the existence of high-density molecular gas. Regarding clump 3, five WISE candidate YSOs identified by OPG13 are projected onto it. This clump has an HCO^+ counterpart (BYF 77c). Clump 2 has an HCO^+ counterpart (BYF 77a) and is coincident with the MSX source G286.3579-00.2933 (identified by CNAV08 as a MYSO candidate), the 2MASS candidate YSO source 10375219-5847133, and two WISE candidate YSOs. For the case of clump 7, a very crowded spot of candidate YSOs appear projected inside its limits. The peak intensity of this clump is almost coincident with the position of

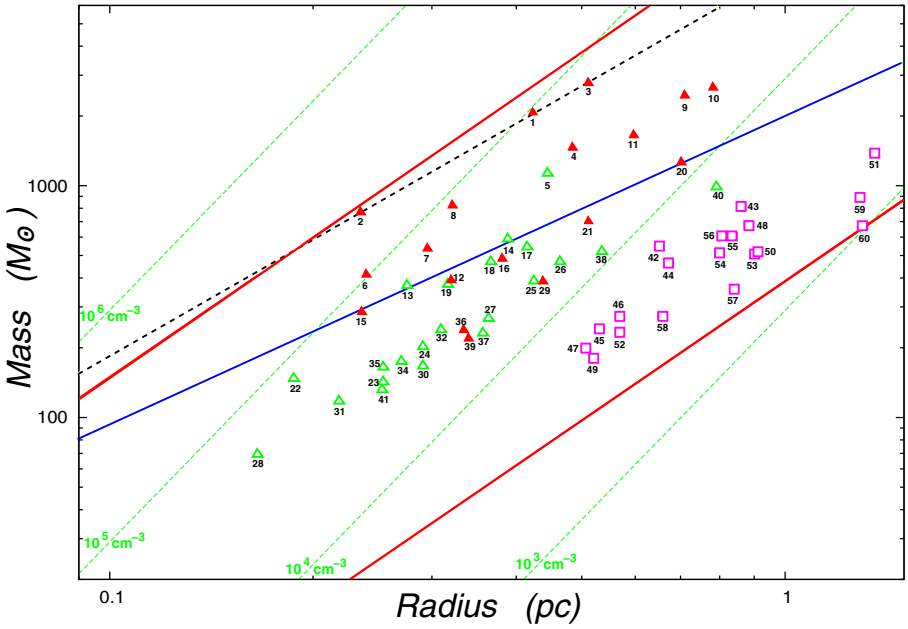

Fig. 9. Mass-radius relationship. Filled red traingles indicate 870 μm clumps with candidate YSOs projected inside the limits determined by `Gaussclumps`, while green open triangles indicate 870 μm starless clumps. Magenta open squares indicate the 250 μm clumps. The blue solid line shows the scaled mass-radius threshold for high-mass star formation determined by Kauffmann & Pillai (2010). The rescaled mass-radius relationship derived by Urquhart et al. (2013) is shown by the dotted black line. Upper and lower solid red lines show surface densities of 1 g cm^{-2} and 0.024 g cm^{-2}, respectively. Dotted green lines indicate volume densities at 10^3 cm^{-3}, 10^4 cm^{-3}, 10^5 cm^{-3} , and 10^6 cm^{-3}.

the MSX CHII candidate G286.1626-00.1877 and the 2MASS sources 10365396-5836293 and 10365749-5836366 (sources 27 and 29 in CNAV08). Three WISE candidate YSOs (OPG13) appear inside the clump. This clump has an HCO$^+$ counterpart (BYF 70b; Barnes et al. 2011). Clumps 6 and 8 are very dense and have HCO$^+$ counterparts (BYF 77b and BYF 67, respectively), although they only have two and one WISE candidate YSOs projected inside their limits. Regarding clump 4, it has an HCO$^+$ counterpart (BYF 70a) and appears projected onto a number of WISE sources, although many of them seem to be located at the inner region of the bubble, outside the molecular gas (see Fig. 8 of OPG13). Clumps 9, 10, and 11 are less dense (they do not have HCO$^+$ counterparts), but a considerable number of WISE candidate YSOs are seen projected inside their limits.

Several clumps with candidate YSOs projected on them lie below the K&P mass-radius relation limit, namely clumps 12, 16, 20, 21, 29, 36, and 39. The most interesting clumps of this sample are probably 12 and 39, since they are located in a region where the star formation activity seems to be very intense (see previous paragraph). Clump 12 has three WISE candidate YSOs projected inside, while clump 39 has six. Both, clumps 12 and 39 have HCO$^+$ counterparts (BYF 70b and BYF 70a, respectively).

3.6. Triggered star formation scenario

As mentioned before, the morphological characteristics of Gum 31 make this nebula a perfect object for the investigation of possible scenarios of star formation. To confirm whether the fragmentation of the collected layer of molecular gas and dust have occurred (as suggested by OPG13 and in Sect. 3.4), we use the analytical model of Whitworth et al. (1994) for the case of an expanding HII region which predicts the time at which the fragmentation occurs. We have followed the analysis of Zavagno et al. (2006), deriving the time when the fragmentation may have occurred ($t_{\rm frag}$), and the size of the HII region at $t_{\rm frag}$ ($R_{\rm frag}$), given by

$$t_{\rm frag} = 1.56\, {a_{0.2}}^{7/11}\, n_3^{-5/11}\, {Q({\rm H^o})^*_{49}}^{-1/11}\ 10^6\ {\rm yr} \quad (7)$$

$$r_{\rm frag} = 5.8\, {a_{0.2}}^{4/11}\, n_3^{-6/11}\, {Q({\rm H^o})^*_{49}}^{1/11}\ {\rm pc}, \quad (8)$$

where $a_{0.2}$ is the isothermal sound speed in the compressed layer, in units of 0.2 km s^{-1} ($a_{\rm s}$/0.2 km s^{-1}); n_3 is the surrounding homogeneous infinite medium into which the HII region expands, in units of 1000 cm^{-3} (n_0/1000 cm^{-3}); and $Q({\rm H^o})^*_{49}$ is the number of ionizing photons, in units of 10^{49} s^{-1} ($Q({\rm H^o})/10^{49}$ s^{-1}). In order to determine $t_{\rm frag}$, in Fig. 10 (upper panel) we compare Eq. (7) with the standard evolutionary model for expanding HII regions developed by Dyson & Williams (1997),

$$R = R_0 \left[1 + a_{\rm HII} \times \frac{t_{\rm dyn}}{R_0}\right]^{4/7} \quad (9)$$

where R is the observed radius of the nebula, $a_{\rm HII}$ is the speed of sound in the ionized medium, and R_0 is the radius of the initial Strömgren sphere (Strömgren 1939) given by

$$R_0[n_0, Q({\rm H^o})] = 3.15 \times 10^{-17}\, n_0^{-2/3}\, Q({\rm H^o})^{1/3}\ {\rm pc}. \quad (10)$$

For the case of NGC 3324, two O 6.5V and one O 8.5 are the main sources of UV photons (see Sect.1), which provide a total ionizing flux of $\sim$1.7 $\times$ 10^{49} s^{-1} (Smith & Brooks 2007). Since about 50 % of the UV photons could be absorbed by interstellar dust in an HII region (Inoue 2001), we adopt a final value $Q({\rm H^o}) \sim 0.85 \times 10^{49}$ s^{-1}.

The upper panel of Fig. 10 shows $t_{\rm frag}$ and $t_{\rm dyn}$ as functions of the initial ambient density n_0. As pointed out in Whitworth et al. (1994), $a_{\rm s}$ = 0.2 km s^{-1} is likely a lower limit for the sound of speed in the collected layer, since both turbulence and extra heating from intense sub-Lyman-continuum photons leaking from the HII region could increase this value. Therefore, in the following we will adopt a range $a_{\rm s}$ = 0.2–0.6 km s^{-1} for the collected layer. For the ionized medium we adopt a value $a_{\rm HII} \simeq 10$ km s^{-1}. Since $t_{\rm dyn}$ is required to be higher than $t_{\rm frag}$ for fragmentation, the initial ambient density in the region where Gum 31 was formed must have been in a range $n_0 \sim$ 950–1800 cm^{-3}. A slightly upper range ($n_0 \sim$ 1100–2500 cm^{-3}) is derived by comparing R with the radius of fragmentation (Fig. 10, lower panel). We have compared these values with the initial ambient density derived using the mass estimates from our 870 μm data and mass estimates from CNAV08. If we assume that all the material observed in the nebula next to the ionization front was swept up during its expansion, an estimate of n_0

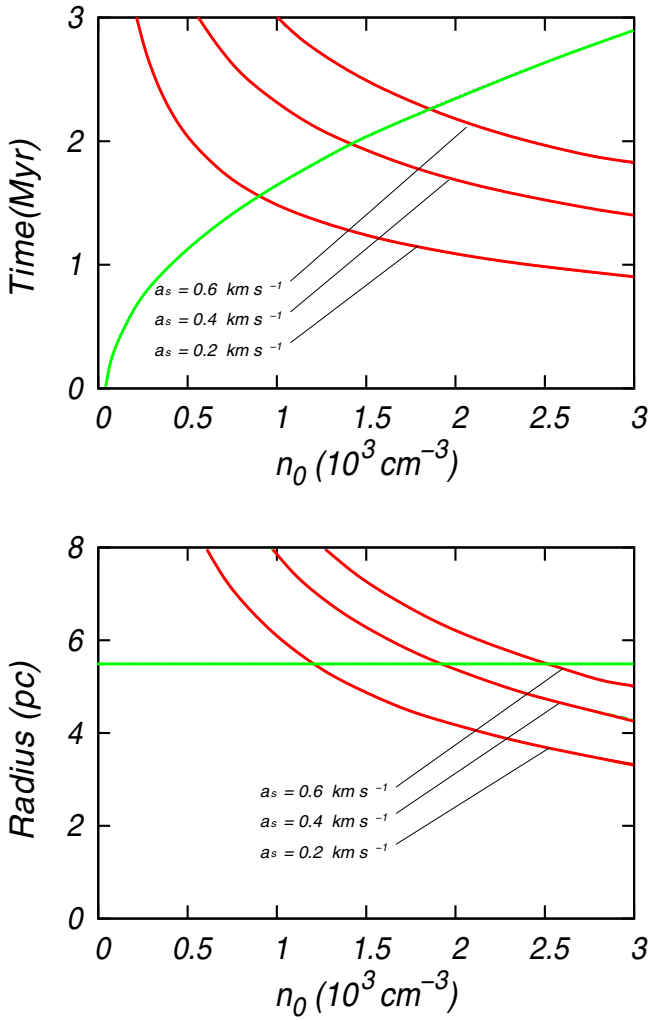

Fig. 10. *Upper panel*: fragmentation time (red curves) and dynamical time (green curve), for R = 5.5 pc as a function of n_0 = 0.2, 0.4, and 0.6 km s^{-1}. *Lower panel*: radius of fragmentation as a function of n_0 for the same values than in the *upper panel* (red curves). The green curve represents the radius of the HII region (5.5 pc).

for Gum 31 can be obtained by assuming that all the gas (either ionized or neutral) was initially located in a sphere of radius equal to that of the HII region (e.g., Zavagno et al. 2007; Cichowolski et al. 2009; Anderson et al. 2015). For the observed radius of the bubble, R, we consider the angular radius of ~7.′5 derived from the radio continuum emission at 843 MHz (CNAV08) which yields R = 5.5 pc at a distance of 2.5 kpc. Considering a total molecular mass of 35 800 $M_\odot$, derived from the 870 μm and 250 μm emission without taking into account the mass of clumps 8, 18, 19, and 35 (see Sect. 3.2) and an ionized gas mass of 2430 $M_\odot$ (at d = 2.5 kpc) associated with the nebula (3500 $M_\odot$ at d = 3 kpc; CNAV08), and R = 5.5 pc, we derive an initial ambient density of $n_0 \sim 2200$ cm^{-3}. This is a lower limit for n_0 since a considerable amount of 870 μm emission outside the clumps and from the center of the nebula was not considered (see Sects. 3.2 and 3.2.2). Furthermore, we do not know if the original parental cloud extended to the current radius of the nebula. The derived value of n_0 is higher than the density limits required for the fragmentation according to the Whitworth et al. scenario, which indicates that the C&C process might be important in the collected layers of molecular gas.

As pointed out by Zavagno et al. (2006), the estimates presented above are rough, since the Whitworth et al. model assumes expansion into a homogeneous medium and many uncertainties remain concerning to the uniformity of the medium where Gum 31 evolved (see Sect. 3.1). In addition, we agree with OPG13 that the presence of cores, bright rims, and pillars at the edge of the bubble suggest that other processes, like the interaction of the ionization front with pre-existing molecular condensation (RDI; Lefloch & Lazareff 1994) or small-scale Jeans gravitational instabilities in the swept-up layers of molecular gas (e.g., Pomarès et al. 2009) could also be active in some regions.

4. Summary

Using LABOCA 870 μm continuum emission and IR and optical archival data, we have carried out a study of the gas and dust adjacent to the Gum 31 nebula. The main results can be summarized as follows:

1. The morphology observed in the 870 μm emission for Gum 31 is typical of many Galactic IR ring nebulae. The emission is strong towards the border of the HII region and faint towards its center, depicting the typical emission of a two dimensional projection of a spherical bubble (i.e. limb brightening effect). The IR emission distribution coincides with that of the molecular gas and suggests that the cold dust and molecular material have been collected behind the ionization front due to the expansion of the nebula. The intense optical, 8 μm, radio continuum, and 870 μm emissions at the west of the powering stars suggest the existence of a PDR at the interface between the ionized and molecular gas. The high intensity in radio continuum, optical, and IR emissions, in the western region of the bubble, as well as the low intensities at the eastern region suggest that the HII region is expanding anisotropically, probably due to the formation of the bubble in an inhomogeneous parental molecular cloud.
2. We have used the `Gaussclumps` algorithm to identify dust clumps adjacent to the nebula. After applying some rejection criteria, we were left with 41 clumps in the 870 μm image. To detect and investigate the dust clumps in the eastern and northestern regions of the nebula, which were not covered in the 870 μm emission data, we made use of an *Herschel* image at 250 μm and we identified 19 clumps.
3. Adopting a distance of 2.5 kpc, the total (gas + dust) clump masses are in the range from 70 $M_\odot$ to 2800 $M_\odot$ and the total mass is about 37 600 $M_\odot$. The deconvolved linear radius derived for the clumps are between 0.12 pc and 1.3 pc. Volume and column densities are in the range from $\sim 1.1 \times 10^3$ cm^{-3} to $\sim 2.04 \times 10^5$ cm^{-3} and 0.4×10^{22} cm^{-2} to 10.4×10^{22} cm^{-2}, respectively. Dust clump temperatures obtained from high-resolution *Herschel* data at 70 μm and 160 μm are between 21 K and 32 K, while dust temperatures at the center of the bubble, close to the ionizing stars of NGC 3324 are as high as ~40 K.
4. We have derived the clump mass distributions for Gum 31, approximated as $\Delta N/\Delta\log(M/M_\odot)$, using different bin sizes, and we fitted a power law $\mathrm{d}N/\mathrm{dlog}(M/M_\odot) \propto M^{-\alpha}$ for each bin size. Obtained spectral indexes are in the range 0.44−1.35, and the weighted mean index is $\alpha = 0.93 \pm 0.28$. The derived spectral index is comparable to other indexes derived in many works from continuum and molecular line data for other regions (e.g., López et al. 2011; Wong et al. 2008). Although the resolution of LABOCA could not be sufficient to make a comparison, the difference between the average slope of the CMDs with the slopes of the stellar IMF

found in the literature suggests that the clumps are not direct progenitors of single stars.

5. The mass-radius relationship for the 41 clumps identified in 870 μm shows that all the clumps lie above the lower surface density threshold for massive star formation of 0.024 g cm^{-2}, while only 15 clumps lie on or above the K&P limit. Of the sample of clumps lying above the K&P threshold, only three of them do not have candidate YSOs projected inside their limits.
6. After analyzing the dynamical age of the HII region and the fragmentation time and radius of the molecular/dust shell surrounding the HII region, we have confirmed that the collect-and-collapse process may indeed be important in the collected layers of gas at the edge of the bubble. The presence of YSO candidates detected by OPG13 and CNAV08 projected onto the 870 μm emission adjacent to the ionization front is a strong indication in favor of this scenario. We keep in mind, however, that other process like radiative-driven implosion or small-scale Jeans gravitational instabilities in the swept-up layers of molecular gas, could also be active in specific regions.

Acknowledgements. We greatefully acknowledge the anonymous referee for her/his helpful comments and suggestions that led to a substantial improvement of this paper. This project was partially financed by CONICET of Argentina under projects PIP 00356, and PIP00107, and from UNLP, 2012−2014 PPID/G002 and 11/G120. N.U.D. acknowledges C. Kramer for his help running `Gaussclumps`, and J. Williams for his help running `Clumpfind`. V.F. acknowledges support from ESO-Chile Joint Committee and DIULS. L.C. acknowledges support from DIULS. L.G. receives support from the Center of Excellence in Astrophysics and Associated Technologies (PFB-06), CONICYT (Chile) and CSIRO Astronomy and Space Science (Australia). M.R. wishes to acknowledge support from CONICYT (CHILE) through FONDECYT grant No. 1140839.

References

Anderson, L. D., Zavagno, A., Deharveng, L., et al. 2012, A&A, 542, A10
Anderson, L. D., Deharveng, L., Zavagno, A., et al. 2015, ApJ, 800, 101
André, P., Men'shchikov, A., Bontemps, S., et al. 2010, A&A, 518, L102
Barnes, P. J., Yonekura, Y., Fukui, Y., et al. 2011, ApJS, 196, 12
Baumgardt, H., Dettbarn, C., & Wielen, R. 2000, A&AS, 146, 251
Beaumont, C. N., & Williams, J. P. 2010, ApJ, 709, 791
Benjamin, R. A., Churchwell, E., Babler, B. L., et al. 2003, PASP, 115, 953
Bergin, E. A., & Tafalla, M. 2007, ARA&A, 45, 339
Bernard, J.-P., Paradis, D., Marshall, D. J., et al. 2010, A&A, 518, L88
Beuther, H., Linz, H., Henning, T., et al. 2011, A&A, 531, A26
Blitz, L. 1993, in Protostars and Planets III, eds. E. H. Levy, & J. I. Lunine, 125
Bock, D. C.-J., Large, M. I., & Sadler, E. M. 1999, AJ, 117, 1578
Brand, J., Massi, F., Zavagno, A., Deharveng, L., & Lefloch, B. 2011, A&A, 527, A62
Cantalupo, C. M., Borrill, J. D., Jaffe, A. H., Kisner, T. S., & Stompor, R. 2010, ApJS, 187, 212
Cappa, C. E., Rubio, M., Martín, M. C., & Romero, G. A. 2009, A&A, 508, 759
Cesarsky, D., Lequeux, J., Abergel, A., et al. 1996, A&A, 315, L309
Churchwell, E., Povich, M. S., Allen, D., et al. 2006, ApJ, 649, 759
Churchwell, E., Watson, D. F., Povich, M. S., et al. 2007, ApJ, 670, 428
Cichowolski, S., Romero, G. A., Ortega, M. E., Cappa, C. E., & Vasquez, J. 2009, MNRAS, 394, 900
Deharveng, L., Lefloch, B., Zavagno, A., et al. 2003, A&A, 408, L25
Deharveng, L., Lefloch, B., Kurtz, S., et al. 2008, A&A, 482, 585
Deharveng, L., Zavagno, A., Schuller, F., et al. 2009, A&A, 496, 177
Deharveng, L., Schuller, F., Anderson, L. D., et al. 2010, A&A, 523, A6
Deharveng, L., Zavagno, A., Anderson, L. D., et al. 2012, A&A, 546, A74
Draine, B. T., Dale, D. A., Bendo, G., et al. 2007, ApJ, 663, 866
Duronea, N. U., Vasquez, J., Romero, G. A., et al. 2014, A&A, 565, A30
Dyson, J. E., & Williams, D. A. 1997, in The physics of the interstellar medium, eds. J. E. Dyson, & D. A. Williams (Bristol: Institute of Physics Publishing)
Egan, M. P., Shipman, R. F., Price, S. D., et al. 1998, ApJ, 494, L199
Elmegreen, B. G., & Lada, C. J. 1977, ApJ, 214, 725
Forte, J. C. 1976, A&AS, 25, 271
Giannetti, A., Wyrowski, F., Brand, J., et al. 2014, A&A, 570, A65
Heiderman, A., Evans, II, N. J., Allen, L. E., Huard, T., & Heyer, M. 2010, ApJ, 723, 1019
Hernandez, A. K., Tan, J. C., Caselli, P., et al. 2011, ApJ, 738, 11
Heyer, M. H., Carpenter, J. M., & Snell, R. L. 2001, ApJ, 551, 852
Hildebrand, R. H. 1983, QJRAS, 24, 267
Hollenbach, D. J., & Tielens, A. G. G. M. 1997, ARA&A, 35, 179
Hosokawa, T., & Inutsuka, S.-i. 2006, ApJ, 646, 240
Inoue, A. K. 2001, AJ, 122, 1788
Jeffers, H. M., van den Bos, W. H., & Greeby, F. M. 1963, Index catalogue of visual double stars, 1961.0
Jenkins, E. B. 2004, Origin and Evolution of the Elements, 336
Kauffmann, J., & Pillai, T. 2010, ApJ, 723, L7
Kauffmann, J., Pillai, T., Shetty, R., Myers, P. C., & Goodman, A. A. 2010a, ApJ, 712, 1137
Kauffmann, J., Pillai, T., Shetty, R., Myers, P. C., & Goodman, A. A. 2010b, ApJ, 716, 433
Kirk, H., Johnstone, D., & Di Francesco, J. 2006, ApJ, 646, 1009
Kovács, A. 2008, in SPIE Conf. Ser., 7020
Kramer, C., Stutzki, J., Rohrig, R., & Corneliussen, U. 1998, A&A, 329, 249
Kroupa, P. 2001, MNRAS, 322, 231
Krumholz, M. R., & McKee, C. F. 2008, Nature, 451, 1082
Lada, C. J., & Lada, E. A. 2003, ARA&A, 41, 57
Lada, C. J., Alves, J. F., & Lombardi, M. 2007, Protostars and Planets V, 3
Lada, C. J., Lombardi, M., & Alves, J. F. 2010, ApJ, 724, 687
Lebouteiller, V., Brandl, B., Bernard-Salas, J., Devost, D., & Houck, J. R. 2007, ApJ, 665, 390
Lefloch, B., & Lazareff, B. 1994, A&A, 289, 559
López, C., Bronfman, L., Nyman, L.-Å., May, J., & Garay, G. 2011, A&A, 534, A131
Maíz-Apellániz, J., Walborn, N. R., Galué, H. Á., & Wei, L. H. 2004, ApJS, 151, 103
McKee, C. F., & Tan, J. C. 2003, ApJ, 585, 850
McLean, B. J., Greene, G. R., Lattanzi, M. G., & Pirenne, B. 2000, in Astronomical Data Analysis Software and Systems IX, eds. N. Manset, C. Veillet, & D. Crabtree, ASP Conf. Ser., 216, 145
Miettinen, O. 2012, A&A, 542, A101
Molinari, S., Swinyard, B., Bally, J., et al. 2010, A&A, 518, L100
Mookerjea, B., Kramer, C., Nielbock, M., & Nyman, L.-Å. 2004, A&A, 426, 119
Motte, F., Andre, P., & Neri, R. 1998, A&A, 336, 150
Motte, F., Schilke, P., & Lis, D. C. 2003, ApJ, 582, 277
Ossenkopf, V., & Henning, T. 1994, A&A, 291, 943
Ohlendorf, H., Preibisch, T., Gaczkowski, B., et al. 2013, A&A, 552, A14 (OPG13)
Ott, S., & Herschel Science Ground Segment Consortium. 2010, Am. Astron. Soc. Meet. Abstr., 216, 413.10
Pomarès, M., Zavagno, A., Deharveng, L., et al. 2009, A&A, 494, 987
Povich, M. S., Stone, J. M., Churchwell, E., et al. 2007, ApJ, 660, 346
Preibisch, T., Roccatagliata, V., Gaczkowski, B., & Ratzka, T. 2012, A&A, 541, A132
Rathborne, J. M., Jackson, J. M., & Simon, R. 2006, ApJ, 641, 389
Romero, G. A., & Cappa, C. E. 2009, MNRAS, 395, 2095
Salpeter, E. E. 1955, ApJ, 121, 161
Samal, M. R., Zavagno, A., Deharveng, L., et al. 2014, A&A, 566, A122
Simon, R., Jackson, J. M., Clemens, D. P., Bania, T. M., & Heyer, M. H. 2001, ApJ, 551, 747
Simon, R., Rathborne, J. M., Shah, R. Y., Jackson, J. M., & Chambers, E. T. 2006, ApJ, 653, 1325
Simpson, R. J., Povich, M. S., Kendrew, S., et al. 2012, MNRAS, 424, 2442
Siringo, G., Weiss, A., Kreysa, E., et al. 2007, The Messenger, 129, 2
Smith, N., & Brooks, K. J. 2007, MNRAS, 379, 1279
Strömgren, B. 1939, ApJ, 89, 526
Stutzki, J., & Guesten, R. 1990, ApJ, 356, 513
Thompson, M. A., Urquhart, J. S., Moore, T. J. T., & Morgan, L. K. 2012, MNRAS, 421, 408
Traficante, A., Calzoletti, L., Veneziani, M., et al. 2011, MNRAS, 416, 2932
Urquhart, J. S., Moore, T. J. T., Schuller, F., et al. 2013, MNRAS, 431, 1752
Vasquez, J., Rubio, M., Cappa, C. E., & Duronea, N. U. 2012, A&A, 545, A89
Vazzano, M. M., Cappa, C. E., Vasquez, J., Rubio, M., & Romero, G. A. 2014, A&A, 570, A109
Walborn, N. R. 1982, AJ, 87, 1300
Watson, C., Povich, M. S., Churchwell, E. B., et al. 2008, ApJ, 681, 1341
Whitworth, A. P., Bhattal, A. S., Chapman, S. J., Disney, M. J., & Turner, J. A. 1994, MNRAS, 268, 291
Williams, J. P., Blitz, L., & McKee, C. F. 2000, Protostars and Planets IV, 97
Wong, T., Ladd, E. F., Brisbin, D., et al. 2008, MNRAS, 386, 1069
Yonekura, Y., Asayama, S., Kimura, K., et al. 2005, ApJ, 634, 476
Zavagno, A., Deharveng, L., Comerón, F., et al. 2006, A&A, 446, 171
Zavagno, A., Pomarès, M., Deharveng, L., et al. 2007, A&A, 472, 835
Zavagno, A., Russeil, D., Motte, F., et al. 2010, A&A, 518, L81